In situ X-ray diffraction and thermal simulation of material extrusion additive manufacturing of polymer

Weiguang Wang [a,*], Yanhao Hou [a], Jiong Yang [a], Zhengyu Yan [b], Fengyuan Liu [c], Cian Vyas [d], Wajira Mirihanage [b,*], Paulo Bartolo [a,d,*]

[a] School of Engineering, Faculty of Science and Engineering, The University of Manchester, Manchester M13 9PL, UK
[b] Department of Materials, School of Natural Sciences, Faculty of Science and Engineering, The University of Manchester, Manchester M13 9PL, UK
[c] School of Electrical, Electronic and Mechanical Engineering, University of Bristol BS8 1TR, UK
[d] Singapore Centre for 3D Printing, School of Mechanical & Aerospace Engineering, Nanyang Technological University 639798, Singapore

ARTICLE INFO

ABSTRACT

Material extrusion additive manufacturing (AM) has gradually become a dominant technology for the fabrication of complex-designed thermoplastic polymers that require a higher level of control over the morphological and mechanical properties. The polymer internal crystal structure formed during the AM process can present significant impacts on the mechanical properties of the individual filaments, as well as the whole structure. Currently, limited details are known about the crystal structure evolution during the material extrusion AM processes of polymers. A novel in situ synchrotron X-ray diffraction (XRD) experimental configuration was developed enabling us to capture the material evolution data throughout the extrusion AM process. The in situ time-resolved data was analysed to reveal nucleation and crystallization sequences during the continuous deposition, with the aid of both complimentary numerical simulations and post-process (ex situ) characterisations. The thermal simulations supported the prediction of the filament temperature profile over time and location during the AM process, while ex situ characterisations validated the correlation between polymer crystallinity (resulting from printing parameters) and corresponding mechanical properties. The results obtained from varied process parameters suggest that the processing temperature has a dominant influence on the crystal microstructure evolution compared to the deposition velocity. A lower processing temperature just above the melting temperature permitted favourable crystallization conditions. The overall analysis demonstrated prospects for enhancing polymer AM, to engineering mechanically hierarchical structures through correlative investigations.

1. Introduction

Additive manufacturing (AM), commonly referred to as 3D printing, is heralding an evolution of manufacturing technology in a wide range of industries. Material extrusion is one of the key AM approaches for polymers due to its affordability, versatility, and simplicity in the printing process. The polymer melt conditions during the extrusion AM and associated solidification process are crucial in determining its final crystalline microstructures which impact to determine the mechanical and functional properties of the fabricated structures [1,2]. As the polymer is extruded in a molten status, it undergoes flow at high shear rates. The material rapidly cools once it leaves the printing nozzle and then is deposited onto the printing substrate. Thermally driven and shear-induced effects are two determining factors for polymer crystallisation during this process, where thermal-induced crystallization presents a more dominant impact that affects the microstructure of polymers [1]. The spherulite size, numbers, distributions and matrix structures during the nucleation and crystal growth are dramatically affected by the temperature-dependent parameters [3,4]. The rate of cooling, which determines the time allowed for polymer chains to move and align into a crystal structure, significantly affects the nucleation density [5,6]. Additionally, the thermal gradient between the solidifying

polymer and the surrounding environment (the printing platform or the previously printed layer), different cooling rates, and degree of undercooling determine the time and rate of molecular mobility [7]. This ultimately influences nucleation and crystallization kinetics, and thus the filament mechanical property, filament-to-filament attachment status, and printed structure morphology. Furthermore, the temperature influences the degree of polymer chain diffusion (reputation) and entanglement at filament interfaces, the weld, which determines the weld strength thus influencing the overall structure's mechanical property. Failure and de-binding of the printed part can occur along with the weld interface of filaments and are particularly evident with mechanical anisotropy at the building direction of a printed structure [8,9]. Therefore, gaining a comprehensive understanding of the thermal behaviour of the filament during the AM process is crucial for studying the temperature-dependent crystallization process. Multiple researchers have conducted polymer crystallization examination research during the material extrusion AM process. For example, researchers have investigated the crystallization behaviours under various conditions, including flow-induced influences [10], isothermal crystallization temperature [11], and the impact of printing parameters [12]. However, the above studies focused less on the crystallization process, specifically the crystallisation that happened during the deposition and printing process, where the thermal behaviour during these processes significantly affects polymer nucleation and crystallization. Therefore, there is a pressing need for novel investigation methods that can address the crystallization process during deposition and printing. In addition, the numerical model has shown promising potential in predicting the crystallization process during the printing process, with several models being developed to forecast temperature profiles during 3D printing [13,14]. However, these models tend to oversimplify the process and provide less accurate results due to their reliance on ideal conditions and coarse mesh models [15,16].

A vast majority of printable polymers are classified as semi-crystalline polymers. For such polymers, the kinetics of crystallization and the final crystal microstructure are highly important to the physical properties of the polymer [17,18]. The characterisation of crystallization kinetics can be determined through X-ray scattering [19,20]. Studies have demonstrated the use of *in situ* synchrotron X-ray diffraction (XRD) during the extrusion of polycaprolactone (PCL) [21,22]. The difference between crystal microstructures and, correspondingly, the mechanical property variations of the PCL filaments have also been studied based on the selected processing parameters. Additionally, the role of processing parameters on crystal structure has also been demonstrated by Northcutt *et al.* using *in situ* Raman spectroscopy to show that the crystallization rate of PCL is faster at higher shear rates and lower temperatures [23].

The mechanical properties of additively manufactured objectives are strongly dependent on the crystalline structure, which can be heavily influenced by the AM process conditions. The understanding of process-structure–property relationships is the key to engineering specific desirable microstructures within the extruded filament and at weld interfaces when considering the material extrusion AM. The enhanced understanding of engineering the crystalline microstructures of additively manufactured polymer components can allow control over not only the shapes but also the properties of such components by controlling the crystalline microstructures. However, the current understanding of crystalline microstructure formation during AM is inadequate to facilitate the engineering of semi-crystalline polymer microstructures during the AM. In particular, relating to the understanding of nucleation and crystal growth characteristics. Thus, extended investigation into the material processing steps involved during polymer AM is required. This study aims to understand how printing conditions such as processing temperature, deposition velocity, and printing substrate influence the polymer crystal nucleation and growth that leads to the as-processed crystalline state. PCL was used as a model semi-crystalline polymer, which is widely employed for bioengineering applications. A novel *in*

situ synchrotron XRD experiment approach was designed to examine a specific material volume during the material extrusion AM process, from within the nozzle to the deposition onto the printing platform (or previously printed layer), and then subsequent cooling. The measurement of crystalline structure evolution was conducted via *in situ* time-resolved XRD as a function of processing temperature and deposition velocities. A multi-stage thermal simulation model was applied to predict the overall temperature evolution in extrusion-based AM. The results from numerical simulations allow to provide the temperature profile and analyse the experimental data to study the crystallization behaviours during deposition, printing and cooling stages. Additionally, post-process *ex situ* calorimetric and mechanical characterisations were also considered to examine the filament tensile strength and crystallinity. Ultimately, results were interpreted in a combined approach for a better understanding of the polymer behaviour during the AM process and thus concluded with several suggestions for future design and AM process optimisation.

2. Experimental setup

2.1. Material and in situ experimental configuration

PCL (Capa^{TM} 6500, Perstorp, Sweden) was selected as a representative semi-crystalline thermoplastic polymer. The material was purchased in pellet form and used directly for printing without any pre-processing procedure. PLA (eSun, China) was considered as the comparison group only examined through *ex situ* approach in order to validate the diversity of the method and reconfirm the correlation between crystallinity and mechanical property. Printed samples were produced through a screw-assisted material extrusion AM system (Fig. 1a) developed in-house [24]. This system was composed of a material heating chamber and a rotational screw chamber. PCL was heated and kept at a molten state in the material chamber and delivered to the screw chamber by compressed air (6 bar). The rotational screw was driven by a stepper motor (Sanyo Denki, Japan) to force the molten material out of a nozzle. The nozzle was fabricated from stainless-steel with an inner diameter of 500 μm. In this study, the screw rotational velocity was kept constant (5 rpm) to guarantee a fixed material flow rate, and processing temperatures were selected as 90 °C and 130 °C for PCL, and 190 °C and 230 °C for PLA (used for *ex situ* test only), due to the material nature. The deposition velocities were selected as 0.65 mm/s and 1.50 mm/s for both materials. The parameters are optimised for achieving the optimal printing quality (extruded filament diameter around 500 μm) while collecting X-ray data with adequate time resolution. The stainless-steel printing platform and pre-printed 3D porous PCL and PLA structure (PCL and PLA filament surface) were selected as different substrates for different printing conditions. 400 μm was set for the layer thickness as well as the initial nozzle-platform distance. These parameters result in eight sets of parameter combinations, simulating different printing conditions from the initial layer printed on the platform, to the following layer-by-layer polymer attachment, as detailed in Table 1. 90 s was set as the experimental time which represents the normal printing and cooling period for a single layer proportional to the size of the fabricated sample.

2.2. Time-resolved X-ray diffraction (XRD)

The *in situ* synchrotron XRD was conducted at the B16 beamline of the Diamond Light Source (Harwell, UK). The schematic setup of the experiment is presented in Fig. 1 (with Supplementary Material Figure S1 presenting the actual configuration). The printing platform (material deposition area) was installed on a controlled motion base to move along the X-axis (through X_1 motion). The screw-assisted extruder together with the motion base was fixed on another controlled motion base that can be moved along the Z-axis. The entire setup was fixed on another motion base (X_2) that can move along the X-axis. Thus, when the
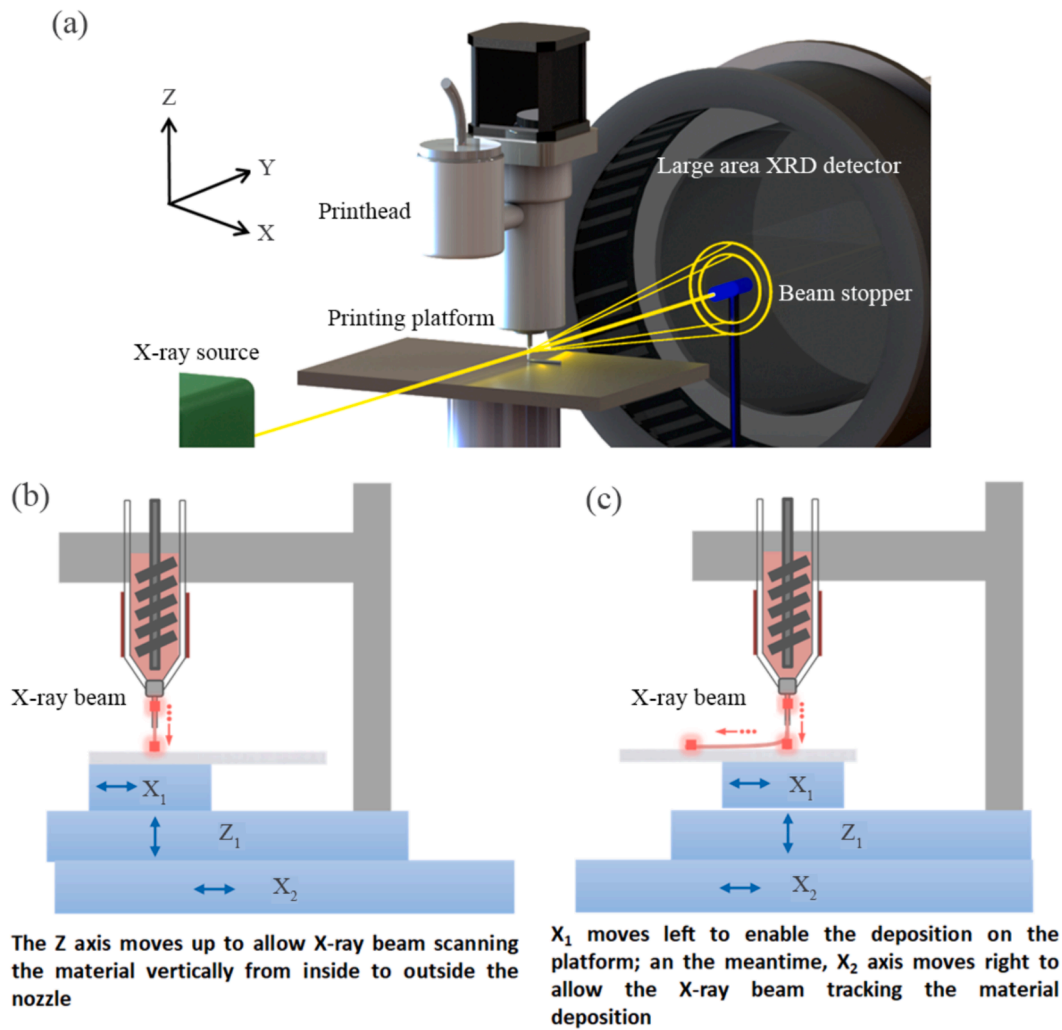
Fig. 1. (a) Schematic experimental system set up of *in situ* time-resolved XRD of the material extrusion AM process, including (b) initial material extrusion and (c) material deposition on the platform.

Table 1
Summary of different combinations of *in situ* AM settings with PCL material.

	Processing temperature	Deposition velocity	Group
Platform (initial layer)	90 °C	0.65 mm/s	A
		1.50 mm/s	B
	130 °C	0.65 mm/s	C
		1.50 mm/s	D
Polymer filaments (following layer)	90 °C	0.65 mm/s	E
		1.50 mm/s	F
	130 °C	0.65 mm/s	G
		1.50 mm/s	H

material was being extruded, the counter motion of the print head enabled the incident unfocused X-ray beam (0.25×0.25 mm^2) with 16.0 keV photon energy to illuminate and follow (lock-on) the same region (volume) of the extruded material. Initially, this would be the vertical movement through the nozzle via the Z-axis movement and then the deposition of the material onto the platform or previously printed layer via combined counter motions of X_1 and X_2. The way that the measurements were designed permitted to record the XRD data from a given fixed volume of material throughout the process which transformed from molten to solid state. A large area XRD detector (Photonic

Science X-ray Image Star 9000® with a 3056 × 3056-pixel array and 31 μm pixel size, Photonic Science, UK) was employed for data collection at 2 Hz with ~0.5 s exposure time. The detector was placed 90 mm away from the sample. The raw data was flat fielded with the background data where no sample group was lit by using ImageJ (NIH, USA).

The integrated diffraction peak intensity, I, from the crystal volume illuminated by the incident beam, can be expressed as [25]:

$$I_{(hkl)} = U_c^{-2} K_{(hkl)} |F_{(hkl)}|^2 V \tag{1}$$

where U_c is the volume of the crystalline unit cell and V is the total volume of the illuminated crystals. $K_{(hkl)}$ is a factor that represents the given (*hkl*) reflection-dependent experimental corrections and physical constants. In this formulation, $|F_{(hkl)}|$ is related to the structure factor. The crystal growth during AM was calculated with a constant filament volume, where the thermal contraction during cooling was neglected. The diffraction data was processed and converted to one-dimensional representation by using Fit2D (European Synchrotron Radiation Facility, France) and compiled with OriginPro (OriginLab. USA).

2.3. Post process calorimetry

The crystallinity (χ_c) of printed PCL and PLA filaments was further evaluated by differential scanning calorimetry (DSC) analysis using a Q100 DSC instrument (TA Instrument, USA). The printed PCL and PLA

filaments were cut into small samples ~ 5 mg, sealed in aluminium pans and lids, and submitted to a nitrogen atmosphere at a flow rate of 50 ml/min. The samples were first heated from −90 °C to 100 °C for PCL and 0 °C to 250 °C for PLA at 10 °C/min and then cooled down from 100 °C to −90 °C for PCL and 250 °C to 0 °C for PLA at 10 °C/min. The temperature was maintained for 2 min, and heated up again from −90 °C to 100 °C for PCL and 0 °C to 250 °C for PLA at 10 °C/min. The first heating cycle shows the thermal history after the AM process, presenting the thermal characteristics of the printed samples. After removing the previous thermal history, the second heating cycle presents the intrinsic thermal properties of the material. The first and second heating curve allows to determine the melting enthalpy (ΔH_m) and χ_c, while the cooling curve allows to determine the crystallization enthalpy (ΔH_c) and χ_c. The χ_c was determined according to the following equation:

$$\chi_c = \frac{\Delta H_m / \Delta H_c}{\Delta H_m^0} \times \frac{100}{w} \tag{2}$$

where, $\Delta H_m / \Delta H_c$ is the experimental melting enthalpy, ΔH_m^0 is the enthalpy of melting of 100 % crystalline PCL (139.5 J/g) and PLA (93 J/g), and w is the weight fraction of PCL and PLA.

2.4. Mechanical tensile evaluation

INSTRON 3344 testing system (Instron, USA) equipped with a 100 N load cell was employed to carry out tensile tests. Samples were extracted from the *in situ* experiments and subsequent processes (following the *in situ* experimental conditions). Samples of 5 mm length were placed in the INSTRON instrument exactly at the centre and stretched in a dry state at a rate of 5 mm/min. The obtained stress–strain data was subsequently analysed following the methodology outlined by Fiedler *et al* [10]. Elastic modulus was determined via linear regression of stress––strain data using the software OriginPro (OriginLab, USA) and the selection of the range was based on the minimization of the linear fitting error.

2.5. Statistical analysis

All experiments were conducted at least three times and the results were presented through the average value with standard deviations. One-way analysis of variance (ANOVA) with *post-hoc* Tukey test was considered using OriginLab (OriginLab Corporation, USA). Significance levels were set at *p < 0.05, **p < 0.01, and ***p < 0.001.

3. Numerical simulation

3.1. Numerical model

Fig. 2a shows the schematic view of a screw-based material extrusion AM system depositing molten polymer on a steel platform. Parts were printed layer-by-layer with molten polymeric filaments being printed on previously cooled filaments. The thermal behaviour during the AM was investigated using computational fluid dynamics simulations using a recently developed modelling approach [26]. The temperature distribution and cooling process were verified by thermal imaging (thermalIMAGER TIM 160S, UK), which allows 1 kHz for fast process to detect the temperature distributions at each time step (0.01 s in experimental work) with good precision. The simulation of material flow inside the cylindrical nozzle is considering ignoring the fluid flow and air compressibility, with molten material exhibiting a laminar flow and no slip between the material and nozzle wall. Non-Newtonian flow behaviour was considered for the material and ideal thermal conditions that the thermal boundaries and material thermal properties remained constant during the deposition and printing process.

The rate of heat energy flow (q) through a unit surface was assumed to be proportional to the negative temperature gradient across it, and described as follows [27]:

$$q = -k \frac{\partial T}{\partial n} \tag{3}$$

where k is the material's thermal conductivity, T = T(x,y,z) and n is the temperature vector field perpendicular to the unit surface and the temperature declination orientation, respectively. The total energy (Q)
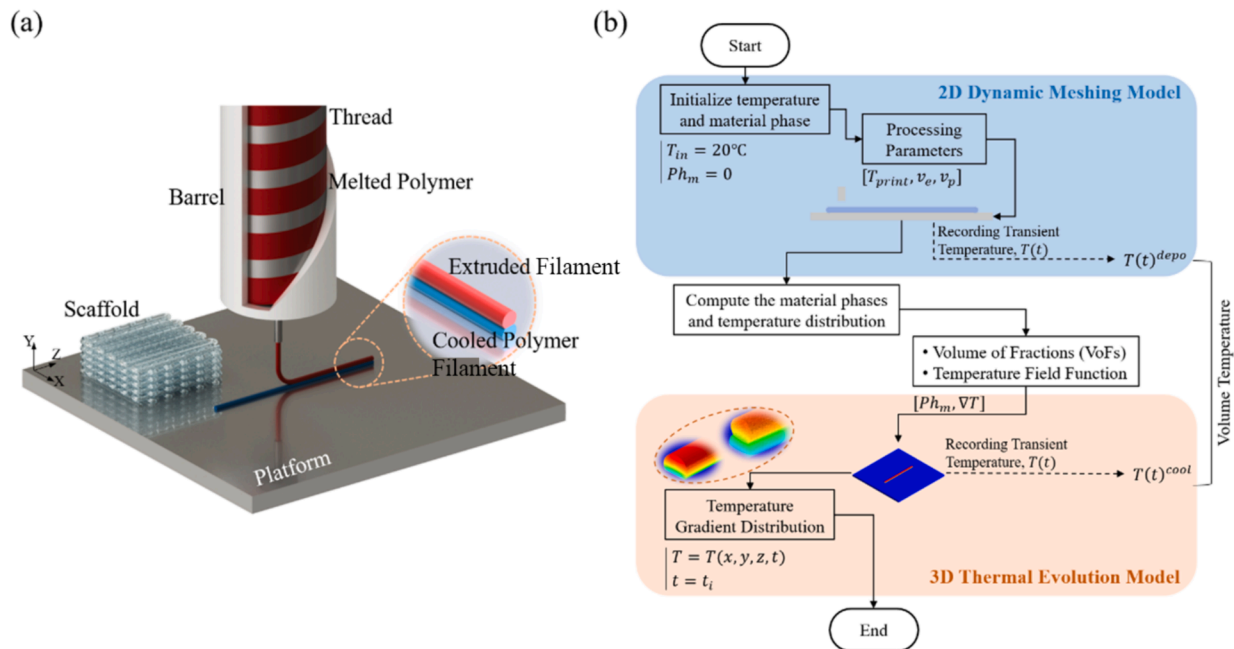

Fig. 2. (a) Schematic view of the AM process based on a material extrusion polymer AM system. (b) The flowchart of the developed multi-stage thermal simulation model. T_{in} is the initial temperature (time at 0 s), T_{print} is the processing temperature, v_e and v_p are the material extrusion and deposition velocity, Ph_m is the material phase (1 represents PCL and 0 represents air).

in a close system with the absence of heat energy generation (the printed filament in our model) is given by Barouh and Mikhailov [28]:

$$Q = \int \Delta T \int_V c\rho \cdot dV \qquad (4)$$

where c and ρ are the specific heat capacity and mass density of the material; and ΔT is the temperature difference. Therefore, the temperature evolution can be obtained as follows:

$$\frac{\partial T}{\partial t} = \frac{k}{c\rho}\nabla^2 T + L_H + Q_v \qquad (5)$$

where Q_v is the volumetric heating source and L_H is the latent heat.

3.2. Multi-stage approach

A multi-stage thermal simulation model has been developed and implemented to evaluate the temperature evolution during material extrusion and cooling [26]. The simulations of printing cases with different processing parameters (temperature and deposition velocity) were implemented in Ansys Workbench (Ansys, USA). Multi-phase models with volume fraction, ideal thermal conditions, and incompressible and non-Newtonian material were considered in the numerical simulations and results were validated by thermal imaging in ref. [26]. Fig. 2b presents a multi-stage thermal simulation model, which combines the models of 2D dynamic meshing and 3D thermal. In the 2D dynamic meshing model, the volume of fractions (VoFs) method was used to track the interface between the material (PCL) and the atmosphere (air). Dynamic meshing allows to simulate the printing process where the shape of the domain changes with time due to motion (nozzle movement) on the domain boundaries. The dynamic meshing was configured to use 50 μm triangles and employed user-assigned parameters (a motion file describes the printing velocities) to control the movement of the nozzle (horizontal displacement) and printing platform (vertical displacement). The temperature and material phase were initialized as 20 °C (ambient temperature) and 0, simulating the atmosphere before printing. Then, different processing parameters were applied to simulate the different considered cases. Melted PCL (processing temperature at 90 °C and 130 °C) was extruded from the nozzle and deposited on the steel platform (cases A-D) or on top of a cooled polymer filament (cases E-H). The 2D dynamic meshing model simulated the material extrusion and deposition process allowing to determine the transient temperature in the volume of interest. After printing one filament, both material phases and temperature distribution were analysed with VoFs and temperature field, and then imported into the 3D thermal evolution model. In the 3D thermal model, the extruded filaments were placed on a printing platform or a cooled filament. Then the evaluation of the subsequent cooling process was completed in the 3D thermal evolution model, which allows the recording of the cooling profile and current temperature gradients at the cross-section of the printed filaments.

3.3. Material parameters and implementation

PCL (Capa^{TM} 6500, Perstorp, Sweden), as detailed above, was considered for this simulation, with the following parameters considered in the numerical model: melting temperature of 336.58 K (63.43 °C, experimentally obtained), density of $1145\,kg/cm^3$, specific heat of $1450\,j/(kg \bullet K)$ and thermal conductivity of $0.14\,w/(m \bullet K)$. A non-Newtonian rheological model was applied to simulate the PCL printing process assuming the following parameters: power law index (n) of 0.39; activation energy of 33.9 kJ/mol [29]; and consistency index of $5.3\,Pa \bullet S^n$ [30]. Additionally, Table 2 summarises the key thermal material properties of the printing platform (stainless-steel) and free space (air). The dimension of the stainless-steel platform in 3D thermal model was $20 \times 30 \times 5\,mm$.

Table 2
The thermal properties of the platform material (stainless-steel) [31] and air [32].

Property	Air	Stainless-steel
Density (kg/m^3)	1.225	8060
Specific Heat $(j/kg \cdot k)$	1006.43	502.42
Thermal Conductivity $(w/m \cdot k)$	0.0242	16.2
Viscosity $(kg/m \cdot s)$	1.7894e-05	/
Heat Transfer Coefficient $(w/m^2 \cdot K)$	10	60

The simulations were performed considering high-performance computing (HPC) cluster (43 nodes of 2 x 16-core Intel Xeon Gold 6130 CPU @ 2.10 GHz + 192 GB RAM+100 Gb/s (4X EDR) mlx5 Mellanox InfiniBand). Triangle elements with 50 μm of size were used in the 2D dynamic meshing model, while for the 3D static meshing model tetrahedron elements were used with 50 μ m of size for the filament and 500 μm of size for both platform and atmosphere area. Time-step size for dynamic meshing was set to 5×10^{-4}s to ensure the regeneration of new meshes at each step during deposition and printing.

4. Results and discussion

4.1. Time-resolved measurements

The *in situ* time-evolved XRD results presented the details of the solidification process of PCL from the molten state to the solid crystalline phase for the initial printed filaments on the stainless-steel platform (samples A-D), as shown in Fig. 3a. A broad scatter was first observed at the beginning of the process when the polymeric material started to be extruded out of the printing nozzle. As a result of the scattering from the molten liquid polymer, this period could be identified as the time prior to nucleation and crystalline solid formation. Therefore, the X-ray signal could be regarded as the scattering that comes from an amorphous melt. Subsequently, the two emerging Bragg peaks (0 2 0) and (1 2 0) from PCL crystals, appeared in the Q range of the detector, indicating the nucleation and solidification of the crystalline material. Here Q = 2π Sinθ/λ, where 2θ is the scattering angle and λ is the wavelength of the incident X-ray beam. The small perturbations on the broad hump continued growing as sharp Bragg peaks as highlighted in Fig. 3a for sample A. Comparing with the broad scatter background, these two peaks ((0 2 0) and (1 2 0)) were much sharper in appearance which corresponds to the formation of well-ordered crystal structures. After the nucleation phase, the crystallization process proceeded, and these two peaks were further developed corresponding to an increase in the crystal volume [19,21]. Then, the peak intensity reached the maximum value, and the peak profile remained stable without further changes. Sharp Bragg peaks over the broad background were observed in all first-layer deposition groups, although the crystallization processes present different trends with various processing temperatures and deposition velocities. Sample A with a lower processing temperature and deposition velocity presented the highest intensity of the sharp peaks, followed by sample C, which shared the same deposition velocity but a higher processing temperature. Samples B and D with higher deposition velocities showed much lower diffraction intensity, and the Bragg peaks were hardly seen in Sample D which has a higher processing temperature.

Fig. 3b summarises the results for the cases where the filaments were printed on top of already printed PCL filaments. In this scenario, crystallization was only evident in the lower processing temperature cases (90 °C). Samples G and H only exhibited the broad peak, and no Bragg peaks were formed, which means the extruded polymer was in the amorphous state. Thus, for the higher processing temperature (130 °C), the crystallization was not observed during a normal printing and cooling period (90 s). Overall, sample E, with a lower deposition velocity and a lower processing temperature, produced the sharpest XRD peak profiles indicating a complete crystallization during the printing
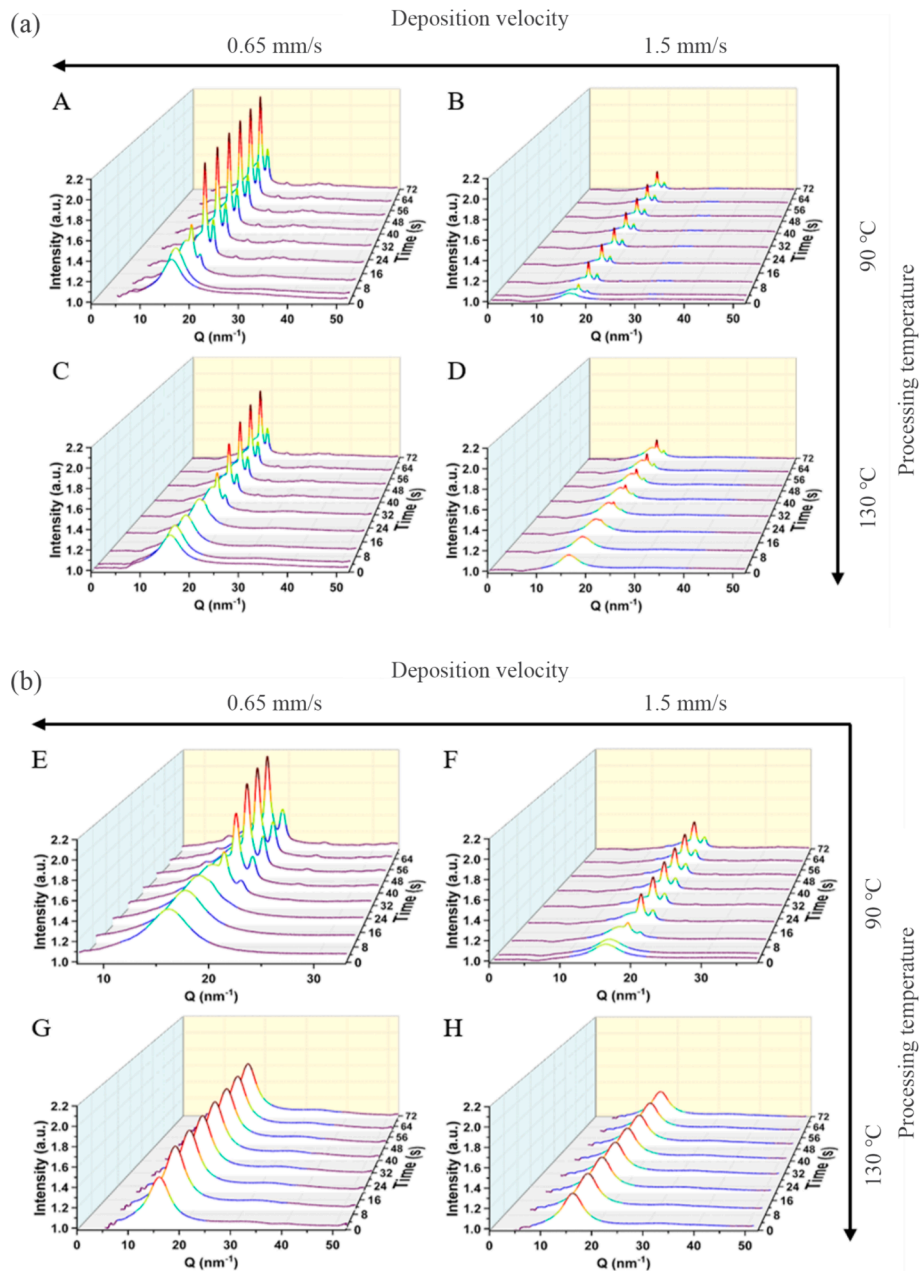
Fig. 3. *In situ* time-resolved XRD results of the (a) initial layer deposition (filaments printed on the stainless-steel platform), and (b) following layer deposition (filaments printed on the PCL structure surface) as a function of processing temperature and deposition velocity.

process. As observed for this case, for the same processing temperature and deposition velocity, both nucleation and crystallization occurred at a later stage in comparison to the case where the filaments were printed directly onto the platform. Generally, samples printed with lower deposition velocities showed comparatively higher diffraction intensity, and the higher processing temperature situation could impede the crystallization process.

4.2. Nucleation and growth

From Fig. 3, it was possible to extract pre-nucleation and crystallization times, as summarized in Fig. 4. As observed, sample B exhibited the shortest pre-nucleation times (3.0 ± 0.5 s) followed by samples A and F (6.0 ± 0.5 s). Contrarily, samples C, D and E showed longer pre-nucleation times with values of 17.5 ± 0.5, 15.5 ± 0.5 and 16.0 ± 0.5 s, respectively. In addition, no sharp Bragg peaks were observed in

samples G and H during the maximum possible *in situ* XRD data capturing period (90 s). This test period is considered in this paper as the pre-nucleation time (Fig. 4).

From Fig. 4, it is possible to observe that the crystallization period presented a similar trend as the pre-nucleation time. Sample B exhibited the shortest crystallization period, lasting for 9.5 ± 0.5 s. Sample A showed a moderate crystallization period of 22.0 ± 0.5 s. Sample F, although under different conditions (different substrates have different thermal removal rates, and different printing velocities may influence the heat dissipation rate [19]), shared a similar moderate crystallization period to sample A. As for sample E, the crystallization period was 42 ± 0.5 s. Similarly, the crystallization took longer time for samples C and D, with values of 51.0 ± 0.5 s and 70.0 ± 0.5 s, respectively.

Comparing A and C, B and D, it is obvious that a lower processing temperature gives shorter pre-nucleation times and crystallization periods. Firstly, lower processing temperature allows the printed filament
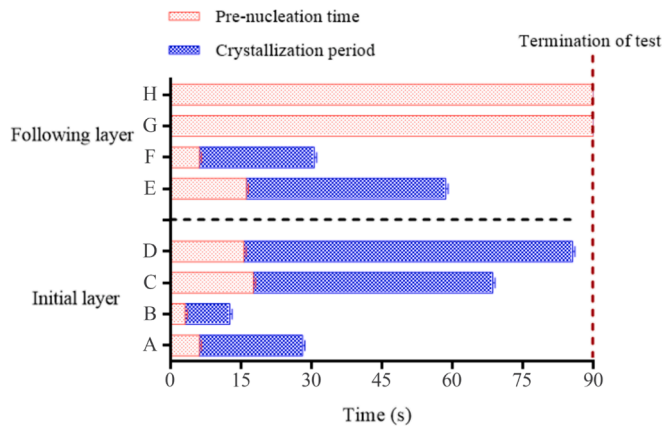
Fig. 4. Time taken nucleation and crystallization. The time until the first XRD appearance is considered as the time for nucleation (pre-nucleation time). The end of the crystallization period is recognized by constant integrated XRD peak intensity.

to cool down in relatively shorter times below its melting point, where crystallization onset is possible. Considering the influence of the substrate (comparing A and E, B and F), the filaments printed on polymer structure exhibited a longer pre-nucleation and crystallization process, almost twice that of the filaments printed on a stainless-steel platform. This is because the polymer has lower heat transfer (dissipation) than the steel, resulting in a longer cooling time.

Fig. 5a and b show the numerically simulated cooling profiles of PCL filaments at different processing conditions. As observed, numerical simulations allowed to estimate the appropriate temperature ranges, where nucleation and crystal growth take place. Some differences between numerical and experimental results can be attributed to the assumptions employed for the model [26]. For example, the boundary condition (heat dissipation) applied in the model, may have a considerable influence on the exact accuracy of the numerical values. Thus, when looking at the specific values such as undercooling, it might be different from the real numerical figure. Nevertheless, it will not impact

the analysis and interpretation of experimental observations.

Nucleation is expected to happen when the temperature is below the melting point with adequate undercooling [6,25]. As indicated by the simulated temperature profiles and the first appearance of the XRD peaks, realistic heterogeneous nucleation requires over 25 °C undercooling (melting point ~ 63.34 °C, obtained from DSC results). For samples A and B, the temperature of the filament cooled to around 38 °C at the corresponding crystallization onset time (6.5 s and 3.0 s), where the required nucleation undercooling of 25 °C. The undercooling of samples C and D were slightly different with a reasonable fluctuation (2 °C) at the crystallization onset time, which may be due to the accuracy of parameters of boundary conditions and material thermal properties in simulation, for example, the heat transfer coefficient. In terms of samples E and F, around 6.0 and 16.0 s XRD peaks started to appear indicating the nucleation and start of the crystallization process. A similar temperature range was observed from the temperature profile (Fig. 5b). In addition, numerical simulations for samples G and H, in which no XRD peaks were visible, indicate that the process conditions prevented these sample volumes from reaching the necessary nucleation undercooling, as even after 90.0 s both sample volumes remained above 40 °C.

When considering material extrusion AM under relatively higher processing temperatures, both the pre-nucleation and crystallization times become longer, as a result of the higher initial heat load carried by a given volume of material that is being printed [20,33]. As suggested by the results, the crystallisation under high temperatures tends to occur even beyond a standard layer-by-layer AM process, especially for samples G and H, no crystallization was observed till the end of the *in situ* data collection period (90.0 s). Slower cooling rates can enable extended periods for polymer chain mobility before the materials reach the glass transition temperature [17,34]. Thus, longer exposure to higher temperatures provides more opportunity for crystals to grow and form higher crystalline volume factions within the fully solidified materials [35]. Nucleation conditions, actual polymer chain mobility at a given temperature and other factors such as shear can also play a significantly role in determining the resulting crystalline volume fraction. Thus, the continuation of the nucleation and crystal growth process throughout this period of high temperature contributes significantly to the mechanical properties [3]. Samples G and H experienced a longer
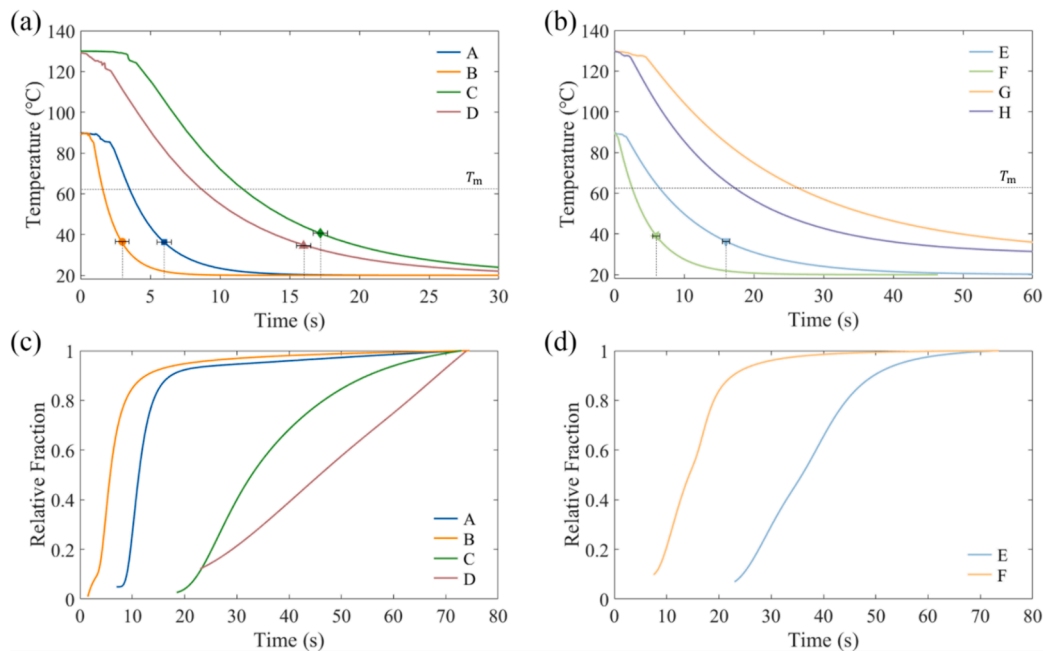

Fig. 5. Temperature profiles of the cooling process based on simulation work for (a) initial layer deposition and (b) following layer deposition. The dashed line (T_m) indicates the melting point of the material. Normalized relative crystal volume fraction evolution during the *in situ* X-ray observations. Plots were derived from integrated XRD peak (0 2 0) intensity (c) initial layer deposition and (d) following layer deposition.

nucleation time and crystallization period. The consequence was the same as sample E when printed at a lower temperature. Results suggested the change of printing substrate from the initial layer (on platform) to the following layers (on polymer) but maintaining the same deposition velocity, a similar thermal condition can still be maintained by reducing the processing temperature. This combination of processing parameters is more suitable for the printing of the first layer (onto the printing platform), as it maintains higher residual heat that potentially to be absorbed by the platform and surrounding environment, thus, avoiding the formation of large crystals [36]. For the printing of the subsequent layers, it would be beneficial to adapt the printing condition similar to sample E, which applied a lower initial heat loading, but the surrounding environment will not rapidly absorb the heat. So, the cooling still allows the formation of smaller crystals for a better mechanical property, but without compromising the layer-to-layer attachment or concern about the bridging effect.

The integrated intensity under a Bragg peak, as detailed by Equation (1), can approximate the crystal volume fraction present in the illuminated volume [37]. Based on this criterion, the integrated peak intensities evolution during the first and subsequent layer deposition are shown in Fig. 5, indicating the relative crystal volume fraction evolution during the process. As observed from Fig. 5c, samples A, B and C showed similar increasing profiles while sample D presented an almost linear type of increase.

Likewise, the integrated peak intensity of the following layer deposition is presented in Fig. 5d. In this case, no crystal growth indication was associated with samples G and H, as no Bragg peak (0 2 0) appeared during the experimental time. The solidification of high-temperature deposition on the following layer was limited to 90 s time with the experimental design. Within this duration, only samples E and F showed crystallization and no crystallization is indicated with samples G and H.

4.3. AM strategies

Comparing the samples from higher deposition velocity (1.50 mm/s) with the lower deposition velocity ones (0.65 mm/s), the diffraction intensities of the lower-velocity samples were much greater than the higher-velocity ones (Fig. 3). According to the experimental results, the lower deposition velocities, enabled favourable crystallization conditions, as further confirmed by calorimetric analysis of final crystal volume fractions (Fig. 6). Generally, lower deposition rates facilitate higher heat dissipation with relatively slower heat build-up. Similarly, the lower processing temperature (90 °C), which allows faster cooling, had a greater diffraction intensity during the early stage of the solidification process. However, they resulted in a relatively lower final crystal volume fraction, possibly due to limited time just below the melting temperature that enables effective crystal growth over a longer time. Compared to the deposition velocity variations, both the experimental and numerical simulation observations indicated a lower processing temperature allows the extruded polymer to nucleate earlier. Lower processing temperatures may enable to reach nucleation undercooling quicker, however, quicker reduction temperature may provide less opportunity for polymer chain folding and thus may end up with lower crystal fractions despite jump start at the beginning. In addition, the printing substrate had limited influence on the final crystal volume fraction although the cases printing on the platform suffered a larger cooling rate and allowed the faster nucleation and crystallization process (Fig. 5). This is more related to the mechanism of polymer chain folding, which drives the crystallization. Normally, a higher temperature can supply the polymer more energy to form the crystalline and the polymer chains are more likely to be broken [34]. However, the influence of material extrusion AM processing parameters on the crystallization process are highly related to each other and cannot be analysed from a single condition. This is also the objective of this research to investigate how the different combinations of processing parameters
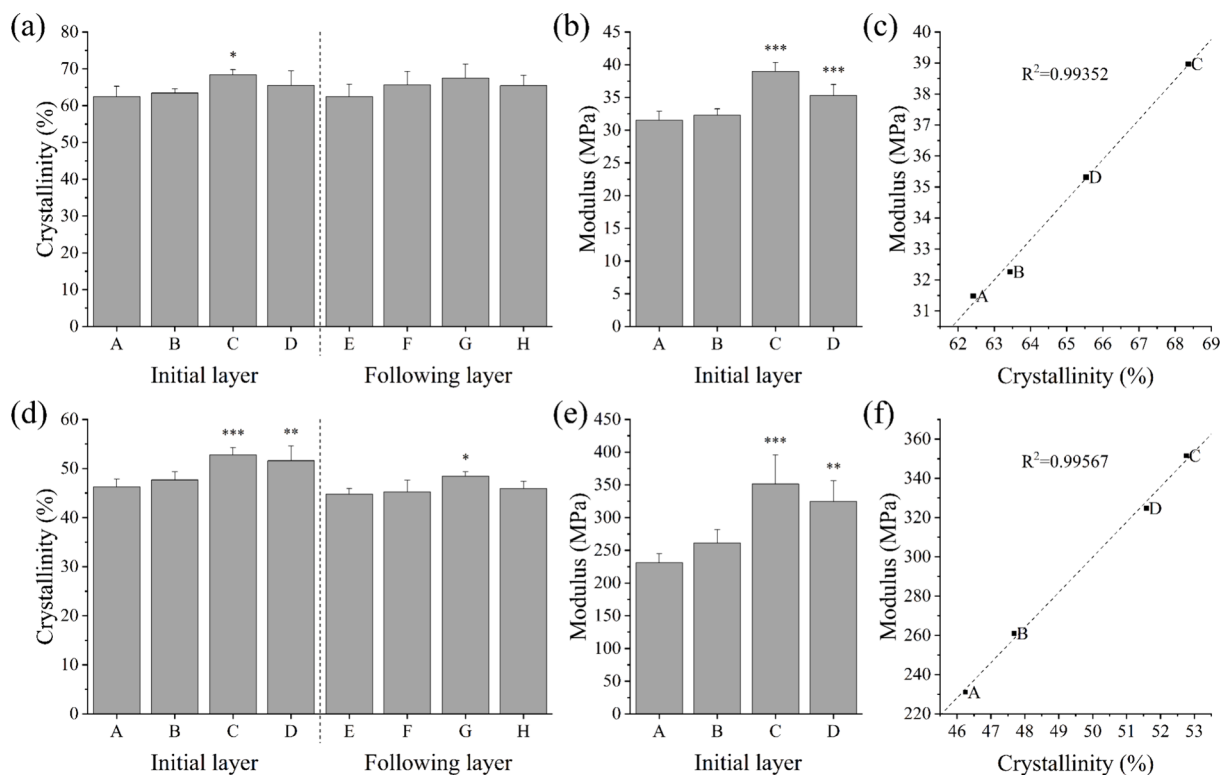

Fig. 6. Crystalline volume fractions of fully processed (a) PCL filaments and (d) PLA filaments. Post-process samples were experimentally examined through calorimetric analysis. Elastic modulus of (b) PCL filaments, (e) PLA filaments, and correlation between crystallinity and elastic modulus of processed (c) PCL filaments and (f) PLA filaments.

influenced the crystallization behaviours. One other point needs to be highlighted here is that the insignificant influence of the shear-induced crystallization [38] according to the experimental observations, as reported similar to previous instances [1]. In general, higher deposition velocities (with a smaller diameter nozzle) introduce higher shear rates which should be favourable for crystallization [39]. However, the experimental data did not indicate such influence from the examined samples. As examined using the simulations, it is evident that the crystallization took place much later than the materials left the nozzle as well as the temperatures were high when the materials were within the nozzle. Thus, it looks like in these scenarios, no apparent impact from shear for crystallization. Overall, the level of crystallization is influential to the mechanical performance of the extruded filaments through the additive process. Thus, the overall crystallization influenced by the processing parameters needs to be considered together with the basic mechanical properties of the polymeric materials.

The elastic modulus of the processed PCL and PLA filaments are also shown in Fig. 6 and the change of the modulus is evident from the data. The modulus related to each processing condition was derived from the tensile testing data. The change in modulus can be attributed to the effect of the crystallinity [40]. The crystallinity restricts the molecular movement of the polymer chains above at a temperature that is higher glass transition temperature, thus, raising the modulus. As a result, the higher the crystallinity, the higher the polymer modulus [41]. A proportional correlation between the elastic modulus and crystallinity was observed in both PCL and ALP and this observation also aligned with other reports [42,43]. The change of processing conditions impacted differently to determine the crystallinity levels between PCL and PLA as observed, but share a similar trend. This attribute is believed to originate from the physical and chemical properties of the material and may need extended studies to understand the trend related to a given material while the main focus of this contribution remains on the processing of PCL through extrusion AM using *in situ* XRD data.

Considering the overall analysis here, sample B indicated a relatively shorter pre-nucleation and crystallization time, which may allow the formation of stronger polymer filaments through smaller crystal sizes due to the extensive generation of nuclei and the formation of crystals.

However, fast cooling and remaining at relatively lower temperatures may result in poor bonding between layers due to the fast solidification. Samples A and F presented a similar crystallization process, which indicated under the same processing temperature, if considering achieving the same polymer microstructural behaviour within the whole product, printing on the platform (the first layer) should be slower while the following layers should be faster. Therefore, a variation of deposition velocity between layers is required to obtain a similar crystallization process. Sample E presented a longer pre-nucleation time and crystallization period due to slower cooling. The slow cooling, which takes a longer time to reach lower temperatures, allows enough time for the printed filament to better bind with the layers.

The development of crystal volume fraction through the suitable cooling process and greater addition between filament layers through retaining higher temperatures can be further considered via a numerically simulated cross-section of first- and second-layer deposition. The temperature gradient distribution was presented in each sample with increasing temperature from the bottom (attached to the platform) to the top region in Fig. 7. As described in the simulation model, the temperature cooling evolution (Equation 6) is highly related to the boundary conditions and the interface between the two materials. The heat transfer coefficient of PCL and air is much smaller than that of stainless steel, resulting in a slower cooling process at the higher positions.

As observed from Fig. 7, samples with slower deposition velocity presented a greater temperature gradient than those with faster deposition velocity, resulting in later nucleation and crystallization onset time and the crystal volume fraction stated to increase slower. However, those samples obtained a higher crystallinity (Fig. 6) due to a warmer ambient temperature, which supplied the polymer with a longer crystallization period. Besides, for the samples with faster deposition velocity and lower processing temperature (samples B and D), the filament has cooled to a lower range close to the ambient temperature (20 °C), presenting a lower temperature gradient distribution (varies from 20 °C to 22.5 °C from bottom to top). Therefore, those two samples have the shortest pre-nucleation and crystallization time, as well as lower final crystal volume fraction, which may result in a poorer mechanical
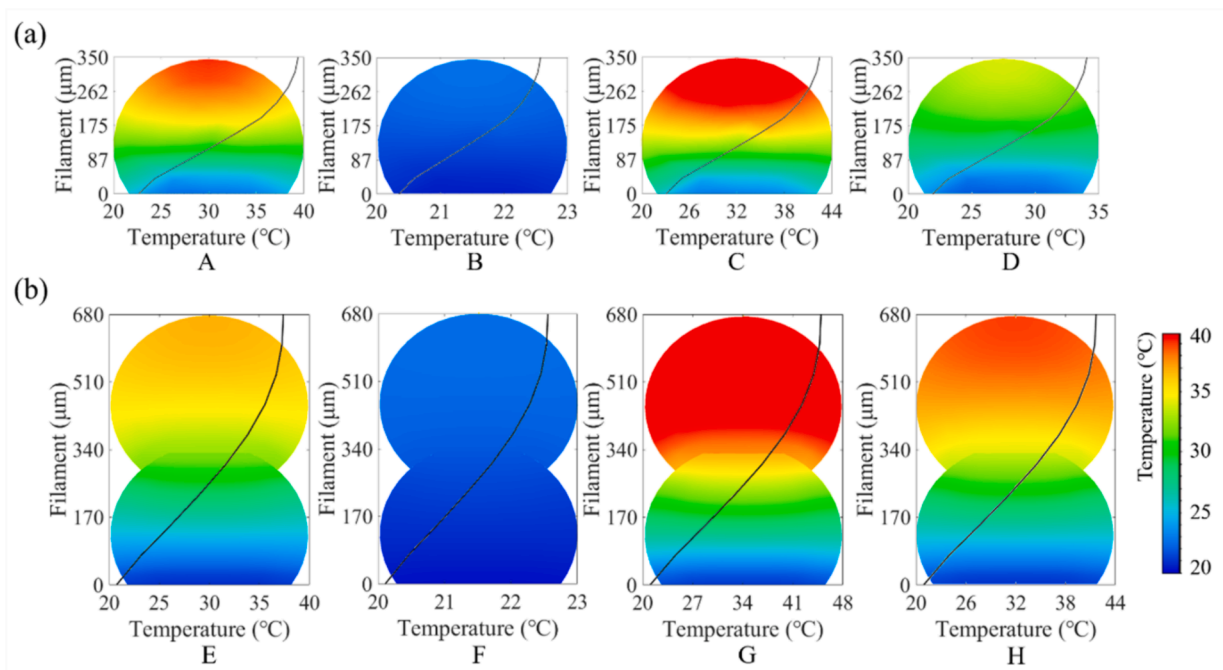

Fig. 7. Temperature distribution at the cross-section of extruded PCL filaments (a) the initial layer (Samples A and B at 7 s, and Samples C and D at 18 s), and (b) the following layer (Samples E and F at 18 s, and Samples G and H at 60 s).

property. In addition, the samples with the same AM settings (processing temperature and deposition velocity) and printed on different substrates shared similar temperature gradients (for the whole filament structure) when crystallization happened. Therefore, the temperature gradient of the second layer (printed on polymer filament) is roughly half that of the first layer, which corresponds to the previous results that the pre-nucleation and crystallization times of those samples (the second layer) were doubled. In addition, the main domain of samples G and H remains over 40 °C during the end of the simulation.

As observed from the temperature gradient distributions at the cross-section of the samples, the bottom region always cools to a lower temperature faster, where the onset of nucleation and crystallization may occur before the top region. This phenomenon may result in the crystallization process performing a gradient variation in the bottom region starts and finishes the crystallization process earlier. However, the cooling process may present the same tendency as the temperature gradient field is formed under the same boundary condition, which results in a hysteresis for the higher region cooling process. This phenomenon can be observed as well on the filament at the longitudinal direction (pre-printed or post-printed).

As we observed here as well as suggested from the previous work, the presence of higher crystal volume fractions tends to provide better mechanical properties [44,45]. However, crystal size distribution, which is an integral attribute of the crystalline volume fraction, is also a paramount consideration for the mechanical properties and performance of the materials, including polymers [21]. Smaller crystal sizes enable enhanced mechanical properties [46]. When process conditions are concerned, lower cooling rates, resulting from higher processing temperatures and slower deposition velocity, can lead to the formation of larger crystals, and thus result in relatively weaker mechanical properties in the printed filament [23], if the analysis is purely based on the crystal size. In this situation, in determining the crystal size (representative average and distribution), understanding of nucleation condition and crystallization time can provide sensible information. Time-resolved experimental limits were attributed to the technical limitations of the instruments employed. This involves the photon flux of the incident X-ray beam, and detector sensitivity which determines the time resolution (at the time of the experiments conducted). In addition, data collection was determined by the system electronics such as storage memory limits. Thus, the moderate extrusion (3D printing) rates were maintained for the experiments to acquire sensible data without blurring by fast transformations associated.

Despite the results indicated here, most commercial polymer 3D printers, especially low-cost equipment that adapt the same combination of processing parameters during the whole AM process, may result in different polymer microstructures between different layers within the same macrostructure. This is not ideal for advanced manufacturing applications, particularly for biomedical engineering and aerospace engineering sectors, where consistent microstructure and macrostructure are both highly required. Also, there appear to be contradictive requirements to acquire better overall mechanical properties for a structure through microstructural optimisation within the filament, and the bonding levels between filaments. In order to reach the enhanced mechanical property of the printed filament, normally a fast-cooling rate is desirable, but when considering continuously printing the filament to fabricate a large-scale structure, the fast-cooling rate can eventually lower the inter-layer filament attachment potential. Thus, to obtain an optimal combination of AM parameters for a uniformed polymer microstructure, when using a fixed material flow rate, it would be useful to print at a relevantly higher temperature and slower deposition velocity for the initial layer. For the printing of the following layers, it would be useful to adopt a relatively lower processing temperature and higher deposition velocity.

Current strategies such as heating the platform can contribute to avoiding warping and enhancing mechanical strength, as well as improving inter-layer binding of material extrusion AM systems.

However, they still present certain limitations when printing large-scale structures. Furthermore, apart from having small crystal microstructures, by developing anisotropic crystal microstructures, it is also possible to selectively modulate the mechanical properties within the same printed polymer structure. However, it needs more demanding thermal and flow control during the material extrusion process. Therefore, future innovations could focus on the integration of a gradient thermal control function, allowing the modulation of polymer microstructure *in situ* during printing. This research is highly relevant to the fabrication of gradient mechanical property structures for aerospace engineering, and the fabrication of additively manufactured bone tissue engineering scaffolds with bespoke properties via controlled crystal microstructures.

5. Conclusions

This work examined different processing conditions of material extrusion AM that influence on PCL crystal microstructure formation through *in situ* time-resolved XRD, with the aid of temperature simulations and post-process thermal analysis. Such understandings can guide achieving optimal material extrusion AM settings with the best nucleation and crystallization conditions, and thus an improved printing quality of the additive-made components, or even modulating the mechanical properties of such additively made components. Results also indicated the limitations that exist in the majority of the current polymer material extrusion AM technologies, where the whole structures are printed with the same combination of AM parameters, which would result in different crystallization levels. Lastly, it was also confirmed that temperature appeared to make the dominant impact on the nucleation and crystallization time compared to the deposition velocity, particularly related to PCL – a material considered in this study. Future work will focus on extended *in situ* studies with wider parameter space and complement post-processing characterization of different materials, potentially allowing to realise appropriate control of the crystallization during the polymer AM.

CRediT authorship contribution statement

Weiguang Wang: Writing – review & editing, Writing – original draft, Supervision, Project administration, Methodology, Investigation, Funding acquisition, Formal analysis, Data curation, Conceptualization. **Yanhao Hou:** Writing – original draft, Visualization, Validation, Investigation, Formal analysis. **Jiong Yang:** Writing – original draft, Visualization, Validation, Software, Investigation, Formal analysis. **Zhengyu Yan:** Writing – original draft, Visualization, Validation, Formal analysis, Data curation. **Fengyuan Liu:** Investigation, Visualization, Methodology. **Cian Vyas:** Investigation, Methodology, Data curation. **Wajira Mirihanage:** Writing – review & editing, Writing – original draft, Supervision, Project administration, Methodology, Investigation, Funding acquisition, Formal analysis, Conceptualization. **Paulo Bartolo:** Writing – review & editing, Writing – original draft, Supervision, Project administration, Methodology, Funding acquisition, Conceptualization.

Declaration of competing interest

Data availability

Data will be made available on request.

Acknowledgement

Appendix A. Supplementary data

Supplementary data to this article can be found online at https://doi.org/10.1016/j.matdes.2024.113255.

References

[1] S.C. Daminabo, S. Goel, S.A. Grammatikos, H.Y. Nezhad, V.K. Thakur, Fused deposition modeling-based additive manufacturing (3D printing): techniques for polymer material systems, Mater. Today Chem. 16 (2020) 100248.

[2] M. Picard, A.K. Mohanty, M. Misra, Recent advances in additive manufacturing of engineering thermoplastics: challenges and opportunities, RSC Adv. 10 (59) (2020) 36058–36089.

[3] J.W. Litwinenko, A.M. Rojas, L.N. Gerschenson, A.G. Marangoni, Relationship between crystallization behavior, microstructure, and mechanical properties in a palm oil-based shortening, J. Am. Oil Chem. Soc. 79 (7) (2002) 647–654.

[4] M. Górny, M. Kawalec, B. Gracz, M. Tupaj, Influence of cooling rate on microstructure formation of Si–Mo ductile iron castings, Metals 11 (10) (2021).

[5] A. Das, J.S. Bryant, C.B. Williams, M.J. Bortner, Melt-based additive manufacturing of polyolefins using material extrusion and powder bed fusion, Polym. Rev. 63 (4) (2023) 895–960.

[6] Y. Lu, D. Lyu, X. Zhao, Y. Men, Influence of molecular weight on the nucleation and growth of different crystal forms in isotactic polypropylene: in situ synchrotron microfocus X-ray scattering combined with fast-scanning chip calorimetry investigations, Macromolecules 56 (7) (2023) 2772–2780.

[7] S.-L. Gao, J.-K. Kim, Cooling rate influences in carbon fibre/PEEK composites. Part 1. Crystallinity and interface adhesion, Compos. A Appl. Sci. Manuf. 31 (6) (2000) 517–530.

[8] C.E. Duty, V. Kunc, B. Compton, B. Post, D. Erdman, R. Smith, R. Lind, P. Lloyd, L. Love, Structure and mechanical behavior of big area additive manufacturing (BAAM) materials, Rapid Prototyp. J. 23 (1) (2017) 181–189.

[9] S. Nathaphan, W. Trutassanawin, Effects of process parameters on compressive property of FDM with ABS, Rapid Prototyp. J. 27 (5) (2021) 905–917.

[10] J.-Z. Liang, The flow-induced crystallization behavior in capillary extrusion of high density polyethylene melts, Polym. Test. 20 (4) (2001) 469–473.

[11] I.A. Reis, P.I. Cunha Claro, A.L. Marcomini, L.H. Capparelli Mattoso, S.P. da Silva, A.R. de Sena Neto, Annealing and crystallization kinetics of poly(lactic acid) pieces obtained by additive manufacturing, Polym. Eng. Sci. 61 (7) (2021) 2097–2104.

[12] N. Momenzadeh, Influences of material extrusion additive manufacturing (MEAM) parameters and additives on polyvinylidene fluoride (PVDF) properties, 2020.

[13] A.M. Jonaet, H.S. Park, L.C. Myung, Prediction of residual stress and deformation based on the temperature distribution in 3D-printed parts, Int. J. Adv. Manuf. Technol. 113 (7) (2021) 2227–2242.

[14] G. Percoco, L. Arleo, G. Stano, F. Bottiglione, Analytical model to predict the extrusion force as a function of the layer height, in extrusion based 3D printing, Addit. Manuf. 38 (2021) 101791.

[15] J. Zhang, X.Z. Wang, W.W. Yu, Y.H. Deng, Numerical investigation of the influence of process conditions on the temperature variation in fused deposition modeling, Mater. Des. 130 (2017) 59–68.

[16] A. El Moumen, M. Tarfaoui, K. Lafdi, Modelling of the temperature and residual stress fields during 3D printing of polymer composites, Int. J. Adv. Manuf. Technol. 104 (5) (2019) 1661–1676.

[17] D. Vaes, P. Van Puyvelde, Semi-crystalline feedstock for filament-based 3D printing of polymers, Prog. Polym. Sci. 118 (2021) 101411.

[18] Z. Jiang, B. Diggle, M.L. Tan, J. Viktorova, C.W. Bennett, L.A. Connal, Extrusion 3D printing of polymeric materials with advanced properties, Adv. Sci. 7 (17) (2020) 2001379.

[19] B.J. Ree, B. Zheng, A. Abbott, L.M. Smieska, K.A. Page, A.R. Woll, Z. Renwick, H. Koerner, Mapping crystallization kinetics during 3D printing of poly(ether ether ketone), Macromolecules 57 (6) (2024) 2810–2817.

[20] A. Nogales, E. Gutiérrez-Fernández, M.-C. García-Gutiérrez, T.A. Ezquerra, E. Rebollar, I. Šics, M. Malfois, S. Gaidukovs, E. Ge¯cis, K. Celms, G. Bakradze, Structure development in polymers during fused filament fabrication (FFF): an in situ small- and wide-angle X-ray scattering study using synchrotron radiation, Macromolecules 52 (24) (2019) 9715–9723.

[21] F. Liu, C. Vyas, G. Poologasundarampillai, I. Pape, S. Hinduja, W. Mirihanage, P. Bartolo, Structural evolution of PCL during melt extrusion 3D printing, Macromol. Mater. Eng. 303 (2) (2018) 1700494.

[22] Y.-T. Hsieh, S. Nozaki, M. Kido, K. Kamitani, K. Kojio, A. Takahara, Crystal polymorphism of polylactide and its composites by X-ray diffraction study, Polym. J. 52 (7) (2020) 755–763.

[23] L.A. Northcutt, S.V. Orski, K.B. Migler, A.P. Kotula, Effect of processing conditions on crystallization kinetics during materials extrusion additive manufacturing, Polymer 154 (2018) 182–187.

[24] F. Liu, W. Wang, W. Mirihanage, S. Hinduja, P.J. Bartolo, A plasma-assisted bioextrusion system for tissue engineering, Cirp Annals-Manuf. Technol. 67 (1) (2018) 229–232.

[25] W.U. Mirihanage, M. Di Michiel, A. Reiten, L. Arnberg, H.B. Dong, R.H. Mathiesen, Time-resolved X-ray diffraction studies of solidification microstructure evolution in welding, Acta Mater. 68 (2014) 159–168.

[26] J. Yang, H. Yue, W. Mirihanage, P. Bartolo, Multi-stage thermal modelling of extrusion-based polymer additive manufacturing, Polymers 15 (4) (2023) 838.

[27] M. Oane, M.A. Mahmood, A.C. Popescu, A state-of-the-art review on integral transform technique in laser-material interaction: Fourier and non-Fourier heat equations, Materials 14 (16) (2021) 4733.

[28] V.A. Barouh, M.D. Mikhailov, One-dimensional heat and mass diffusion modelling software, App. Math. Model. 13 (10) (1989) 568–573.

[29] N. Noroozi, L.L. Schafer, S.G. Hatzikiriakos, Thermorheological properties of poly (ε-caprolactone)/polylactide blends, Polym. Eng. Sci. 52 (11) (2012) 2348–2359.

[30] B. Zhang, S.H. Chung, S. Barker, D. Craig, R.J. Narayan, J. Huang, Direct ink writing of polycaprolactone / polyethylene oxide based 3D constructs, Prog. Nat. Sci.: Mater. Int. 31 (2) (2021) 180–191.

[31] E. Edge, Thermal properties of metals, conductivity, thermal expansion, specific heat. https://www.engineersedge.com/properties_of_metals.htm.

[32] T.E. ToolBox, Air - Thermophysical Properties. https://www.engineeringtoolbox.com/air-properties-d_156.html.

[33] T.A. Ezquerra, A. Nogales, M.C. García-Gutiérrez, E. Rebollar, O. Gálvez, I. Šics, M. Malfois, Probing structure development in Poly(vinylidene Fluoride) during "operando" 3-D printing by small and wide angle X-ray scattering, Polymer 249 (2022) 124827.

[34] C. Yang, X. Tian, D. Li, Y. Cao, F. Zhao, C. Shi, Influence of thermal processing conditions in 3D printing on the crystallinity and mechanical properties of PEEK material, J. Mater. Process. Technol. 248 (2017) 1–7.

[35] W. Wang, G. Zhao, X. Wu, Z. Zhai, The effect of high temperature annealing process on crystallization process of polypropylene, mechanical properties, and surface quality of plastic parts, J. Appl. Polym. Sci. 132 (46) (2015).

[36] Y. Furushima, C. Schick, A. Toda, Crystallization, recrystallization, and melting of polymer crystals on heating and cooling examined with fast scanning calorimetry, Polym. Crystall. 1 (2) (2018) e10005.

[37] Z. Yan, A. Abdelkader, S. Day, C. Tang, C. Casiraghi, W. Mirihanage, In situ probing of the thermal treatment of h-BN towards exfoliation, Nanotechnology 32 (10) (2021) 105704.

[38] Ž. Górecka, J. Idaszek, D. Kołbuk, E. Choińska, A. Chlanda, W. Święszkowski, The effect of diameter of fibre on formation of hydrogen bonds and mechanical properties of 3D-printed PCL, Mater. Sci. Eng. C 114 (2020) 111072.

[39] A. Jabbarzadeh, R.I. Tanner, Flow-induced crystallization: unravelling the effects of shear rate and strain, Macromolecules 43 (19) (2010) 8136–8142.

[40] Y. Hou, W. Wang, P. Bartolo, Investigation of polycaprolactone for bone tissue engineering scaffolds: in vitro degradation and biological studies, Mater. Des. 216 (2022) 110582.

[41] L. McKeen, 3 - Introduction to the Physical, Mechanical, and Thermal Properties of Plastics and Elastomers, in: L. McKeen (Ed.), The Effect of Sterilization on Plastics and Elastomers (third Edition), William Andrew Publishing, Boston, 2012, pp. 57–84.

[42] Q. Liu, S. Yuan, Y. Guo, A. Narayanan, C. Peng, S. Wang, T. Miyoshi, A. Joy, Modulating the crystallinity, mechanical properties, and degradability of poly (ε-caprolactone) derived polyesters by statistical and alternating copolymerization, Polym. Chem. 10 (20) (2019) 2579–2588.

[43] L.R. Middleton, S. Szewczyk, J. Azoulay, D. Murtagh, G. Rojas, K.B. Wagener, J. Cordaro, K.I. Winey, Hierarchical acrylic acid aggregate morphologies produce strain-hardening in precise polyethylene-based copolymers, Macromolecules 48 (11) (2015) 3713–3724.

[44] E. Su, G. Bayazit, S. Ide, O. Okay, Butyl rubber-based interpenetrating polymer networks with side chain crystallinity: self-healing and shape-memory polymers with tunable thermal and mechanical properties, Eur. Polym. J. 168 (2022) 111098.

[45] W. Hu, The physics of polymer chain-folding, Phys. Rep. 747 (2018) 1–50.

[46] M.R. Abu Bakar, Z.K. Nagy, A.N. Saleemi, C.D. Rielly, The impact of direct nucleation control on crystal size distribution in pharmaceutical crystallization processes, Cryst. Growth Des. 9 (3) (2009) 1378–1384.